Understanding the role of rubidium in multiple-cation based high efficiency perovskite solar cells

Pankaj Yadav, M. Ibrahim Dar, [*] *Neha Arora, Essa A. Alharbi, Fabrizio Giordano, Shaik Mohammed Zakeeruddin, Michael Grätzel*

Dr. P. Yadav, Dr. M. I. Dar, Dr. N. Arora, E. A. Alharbi, Dr. F. Giordano, Dr. S. M. Zakeeruddin, Prof. M. Grätzel
Laboratory of Photonics and Interfaces, Institute of Chemical Sciences and Engineering, École Polytechnique Fédérale de Lausanne, CH-1015-Lausanne, Switzerland.

E-mail: ibrahim.dar@epfl.ch

Over the last few years, perovskite solar cells (PSC) have gained considerable attention because of the upsurge in their power conversion efficiency (PCE). [1-3] The favorable optoelectronic properties of perovskite material, like high absorption coefficient, long charge carrier diffusion length, tunable bandgap, low binding energy of excitons and high charge carrier mobilities led to a rapid increase in the performance of PSCs. [3-5] Typically, PSCs are fabricated by sandwiching the perovskite absorber layer between the electron and hole selective transport layers. The selective contacts are chosen in a way to obtain ideal band alignment, low interfacial recombination, and efficient charge collection. [6,7] Tremendous efforts have been devoted towards investigating the electron and hole transport layers (ETL and HTL), such as TiO_2, PCBM, PTAA and spiro-OMeTAD, etc. [8-11] Of the various selective contacts, TiO_2 (ETL) and spiro-OMeTAD (HTL), have been widely explored. Along with finding the suitable ETL and HTL, a significant attention has been devoted towards altering the interfacial characteristic by doping or engineering the selective contacts to facilitate better charge transport. [12-15] However, in the literature a few

1

reports discuss the influence of variations in the intrinsic property of the absorber material on the interfacial properties and the overall performance of the PSC.

Even though the performance of PSCs have reached beyond 22%, these cells suffer from the hysteresis when the net terminal current-voltage (J-V) response is measured in the forward and backward directions. [16-18] Various approaches, including the optimization of ETL and HTL, passivation of ETL and HTL surfaces, or adoption of inverted structure, etc. have been used to reduce the hysteresis in PSCs. [19-22] However, to the best of our knowledge, a detailed investigation regarding the impact of the chemical composition of perovskite layer on the hysteresis of devices has been rarely carried out. To address these important points, in the present study, we explore the role of cesium (Cs) and rubidium (Rb) cations on the interfacial property in complete devices by examining the transport and recombination processes using J-V characteristics and impedance spectroscopy. As the reliability of these measurements depends on the performance of devices, we have chosen two different PSCs (MAFACs)Pb(IBr)$_3$ (MA=CH$_3$NH$_3^+$, FA=CH(NH$_2$)$_2^+$) and (MAFACsRb)Pb(IBr)$_3$ denoted as device A and device B, respectively, yielding an impressive PCE of 19.5% and 21.1%, respectively. [23,24] For details, see the experimental section. We further extended this comparative study to investigate the hysteresis phenomena in both solar cells using the capacitive response calculated using J-V characteristics in the dark as a function of scan rate and the capacitance measured as a function of frequency.

Figure 1 illustrates the cross-sectional SEM image of both devices displaying various layers and interfaces comprising the PSC. The compact and mesoporous layers of TiO$_2$ deposited, respectively, via spray pyrolysis and spin coating method are covered with an absorber layer of (MAFACs)Pb(IBr)$_3$ (Figure 1a) or ((MAFACsRb)Pb(IBr)$_3$ (Figure 1b). Spiro-OMeTAD as a hole selective layer and a ~70 nm gold (Au) layer as a back contact were deposited using spin-coating and thermal evaporation methods, respectively. For details, see the experimental section.
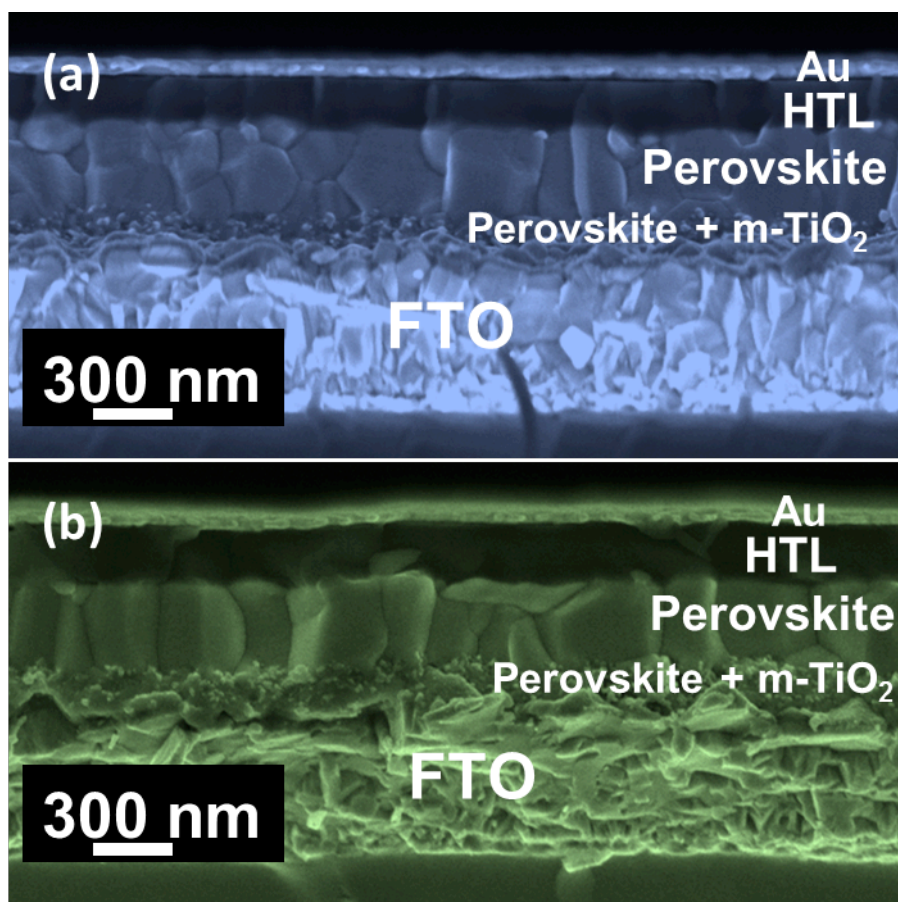
Figure 1. (a) Morphological analysis: Cross-sectional SEM micrograph of (b) triple cation based device (Device A), and (b) quadruple cation based device (Device B) displaying various layers.

Figure 2a depicts the J-V characteristics of device A and B collected under AM1.5 simulated illumination. The device A exhibits an open circuit voltage (V_{OC}) of 1.12 V, short circuit current density (J_{SC}) of 22.8 mA/cm^2, *FF* of 75% and a PCE of 19.5%, whereas device B shows V_{OC} of 1.16 V, J_{SC} of 22.9 mA/cm^2, *FF* of 78%, and PCE of 21.1%. High values of V_{OC} and *FF* extracted from the J-V characteristics signify that the contacts are highly selective.

To investigate the critical characteristics, such as effective ideality factor, open circuit voltage, and built up voltage of the triple and quadruple cation based PSCs, we systematically characterized both devices by various techniques. The dark J-V characteristics for both devices shown in the inset of Figure 2a, illustrate the exponential behaviour, which is

commonly given as $J_d = J_0 \left[exp\left({qV}/{mk_BT} \right) - 1 \right]$ where, J_0 is the reverse saturation current,

q, k_B and T are elementary charge, Boltzmann constant and cell temperature, respectively.
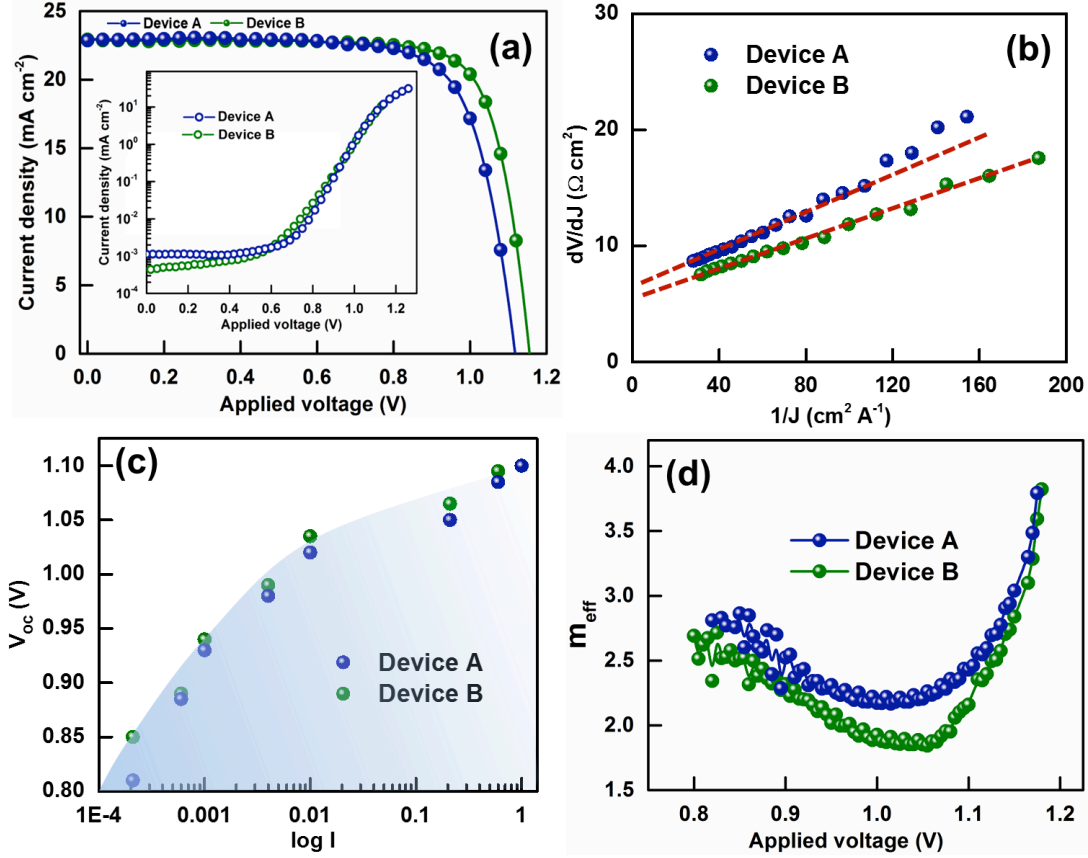

Figure 2. (a) J-V characteristics of the triple (Device A) and quadruple (Device B) cation based perovskite solar cells recorded under standard illumination; inset shows dark J-V characteristics, (b) plot of -dV/dJ versus 1/J curves; solid lines represent the linear fitting, (c) open circuit voltage of the devices measured under various illumination levels, and (d) effective diode ideality factor as a function of applied voltage.

To calculate the series resistance (R_S) and ideality factor (m) for both solar cells, we plotted *dV/dJ vs. 1/J* (Figure 2b) (in case of illumination, *dV/dJ* is plotted against 1/(J-J_{sc})). Symbols in Figure 2b represent the experimental data calculated by taking the derivative of the above equation and plotted in the high forward bias region. The line in Figure 2b shows a linear fit of the experimental data, where the intercept on *y*-axis and the slope yields the values of R_S and *m*, respectively. [25,26] The values of R_S obtained for the device A and B are 8.1 and 6.7 Ω, respectively. As both devices were fabricated in a same batch using the same

architecture, i.e., compact layer, blocking layer and HTM, the apparent difference in the value of R_S could be attributed to the variation in the inherent conductivity of perovskite material. Therefore, we infer that an extra cation, i.e., Rb incorporated into the perovskite film increases the conductivity by lowering the value of R_S in device B, which consequently increases the FF as $FF = FF_0(1 - R_S)$. However, other possible factors, such as modulation of band alignment at the perovskite-TiO$_2$ and perovskite-spiro-OMeTAD interfaces could also contribute to Rs. The values of m estimated for the device A and B are 1.91 and 1.84, respectively. Relatively lower value of m could justify the higher photovoltage yielded by the device involving Rb containing perovskite films.

Figure 2c shows the open circuit voltage of both devices measured under different illuminations ranging from 2×10^{-3} to 1 sun. The two independent regimes in the V_{oc} vs. $log\ I$ plots imply the occurrence of different charge carrier recombination mechanisms with respect to the illumination intensity. [27] An average value of the ideality factor (m_0) is calculated for both solar cell in two regions. Under low light intensity, the device A and B show an average m_0 value of 1.8 and 1.6, respectively, and in the higher range of $log\ I$, the values of m_0 slightly increase to 1.95 and 1.8, respectively. The value of $m_0 > 1$ signifies the dominance of trap-assisted recombination, which is slightly higher in case of device A than device B. [28,29] These results establish that an extra cation, i.e., Rb incorporated into the films reduces the trap-assisted recombination along with increasing the conductivity of perovskite material.

To get further insights into the recombination mechanism, the effective value of ideality factor over an applied bias range was calculated from the dark J-V characteristics (Figure 2a) using the expression $m_{eff} = kT/q\left(dV/d\ln(J)\right)$, where V represents the local quasi Fermi level splitting within the perovskite material. In the present calculation, it is necessary to distinguish the role of R_{SH}, because in the low forward bias region, $J \approx V/R_{SH}$ yields the above expression as $m_{eff} = qV/k_BT$ which is essentially not related to the diode

5

characteristics. Figure 2d shows the bias dependent values of m_{eff} for both devices. The trend obtained for both solar cells shows a saturated response near the bias close to the open circuit potential, which is consistent with the work reported by Kirchartz et al. [28,30] The value of m_{eff} close to 2 for both devices implies that recombination behavior is dominated by trap-assisted (Shockley–Read–Hall (SRH)) type recombination. The variation in the ideality factors calculated using two different methods (Fig. 2 (c) and (d)) could arise from the difference in the Fermi level splitting, which happens due to illumination in one case (Fig. 2 (c)) while in the other case (Fig. 2 (d)) it occurs due to the applied bias. A significant difference in the ideality factors under low illumination as compared to high illumination could arise from an improper splitting of the Fermi levels. It is also known that the transport of electrons and holes, respectively, in TiO_2 and spiro-OMeTAD, and the carrier recombination within the device influence the FF. To identify an interplay between the recombination and transportation phenomena in the devices, we fitted the high forward bias region through $J \propto V^n$; where n is the asymptotic exponent. The obtained value of the asymptotic exponent close to 2 for both devices signifies the same quality of TiO_2 and spiro-OMeTAD, and is not limited by the transport mechanism. Therefore, FF in the device A is mainly limited by the recombination mechanism and high R_S.

We further studied the impact of composition on the charge transport, recombination resistance, and the resistive and capacitive components of various interfaces using impedance spectroscopy (IS). These parameters play a crucial role in elucidating the photovoltaic performance of the solar cell. IS spectra (Figure 3) for both solar cells were recorded at room temperature (25°C) in the dark at different applied bias (0-1.2 V). The frequency range of 1-100 kHz with an ac perturbation signal of 20 mV was employed in all the IS measurements. Figure 3 presents the experimental Nyquist spectra for both solar cells. A simplified circuit was used to fit the impedance spectra (see SI). A series resistance R_S represents the resistance offered by FTO, connecting wires and gold contacts. Z_{HF} impedance element, which is due to

the selective contacts or their interface with the absorber layer, has been employed to fit the high frequency spectra. In addition, a constant phase element (CPE) is used instead of pure capacitance. Finally, the low frequency spectrum which is due to the impedance of perovskite material has been assigned to Z_{LF}, which is combination of recombination resistance and chemical capacitance in parallel. [31-33] The complete set of IS spectra obtained for both devices follows the same trend, while the magnitude of various resistive and capacitive components is different (SI).
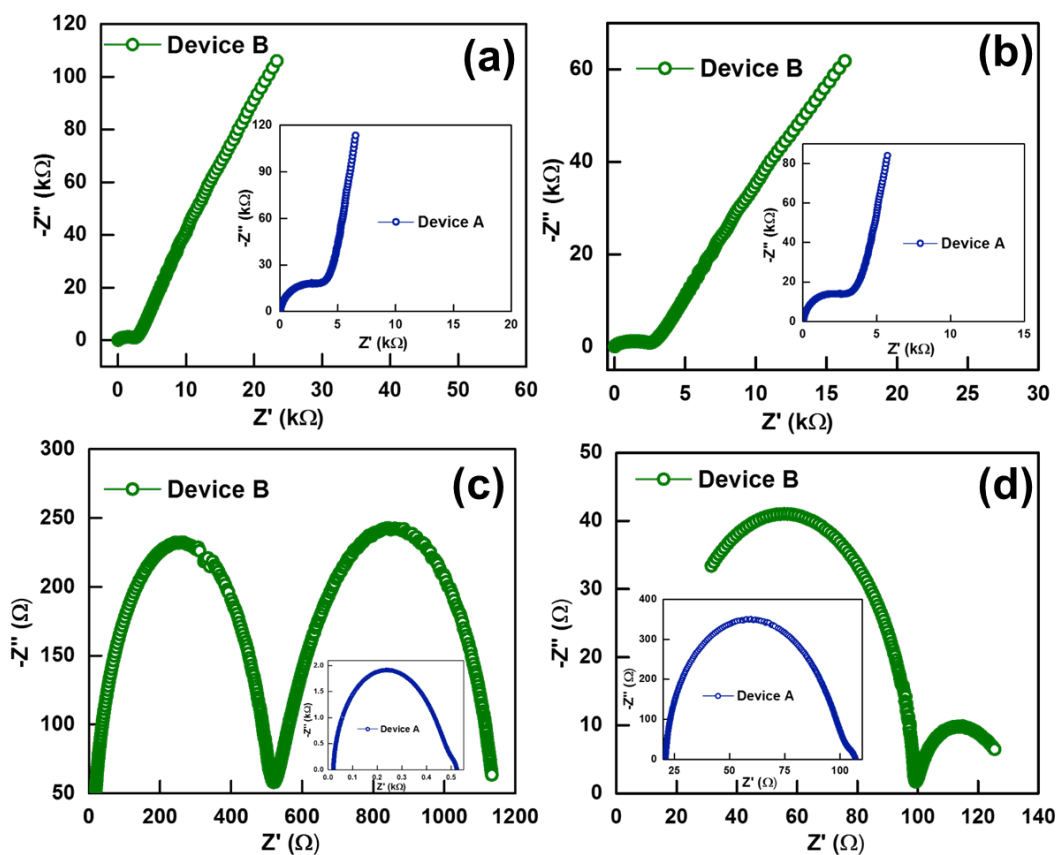

Figure 3. Nyquist spectra obtained from the triple (Device A) and quadruple (Device B) cation based perovskite solar cells at (a) zero bias, (b) mid forward bias (less than knee voltage), (c) knee voltage, and (d) open circuit voltage.

The plot in Figure 3a and 3b corresponds to the zero and moderate forward bias (below knee voltage, which is 850 mV for the device A and 900 mV for the device B) for both devices. The IS spectra for both devices feature two distinguished responses at the low and high frequency. A low frequency arc is followed by a high frequency semicircle which is

mainly related to the transport characteristics in spiro-OMeTAD. The comparable value of the high frequency semicircle in both solar cells signifies the same quality of spiro-OMeTAD deposited during the fabrication process. By closely evaluating the IS spectra from the low forward bias to the knee voltage, a clear signature of the transmission line (TL) is missing. The absence of the TL behaviour indicates a fast transport of electrons in both devices, therefore transport cannot be considered a performance limiting factor. With an increase in the applied bias towards the knee voltage of the corresponding devices (Figure 3c), the high frequency spectra do not show any significant change in the magnitude, further confirming the assignment of the high frequency spectra to the charge transport in spiro-OMeTAD. Previously, it has been shown that the absence of spiro-OMeTAD or the dominance of electron transport causes a significant change in the high frequency spectra when the bias across this interface was increased. [34]

With a gradual increase in the applied bias from the knee voltage to the V_{OC} of the corresponding devices (1.12 V for the device A and 1.16 V for the device B), (Figure 3c and d), a change in the magnitude of the high frequency spectra is observed in addition to the formation of semicircle at the low frequency. As compared to the device A, device B shows a significant change in the high frequency spectrum, which infers a better charge transport across HTM/perovskite interface. In both devices, the rate of change in the low frequency spectrum is higher as compared to the high frequency spectrum. [33,34] The decreasing trend in the high and low frequency spectra is continuous for both devices when the applied bias increases towards the V_{OC} of the solar cell. The IS spectrum at a V_{OC} of the corresponding solar cell is mainly dominated by the high frequency spectrum.

Another important phenomenon occurring within the PSC is the recombination rate which is inversely proportional to the recombination resistance (R_{rec}), and has been estimated by fitting the IS spectra at the low frequency. The electronic equivalent circuits used to fit the IS experimental data are shown in Figure S2. Figure 4a shows the comparison of R_{rec} as a

function of applied bias for both devices. From the R_{rec} plot, a higher value of R_{rec} for the device B signifies the lower recombination rate, which arguably supports higher value of V_{OC}. [34] Figure 4b shows the Mott-Schottky plots recorded at 500 Hz for both devices. The high value of intercept on the *x*-axis establishes high built-in potential for device B than device A, which is in agreement with high V_{OC} yielded by the former device. [35]
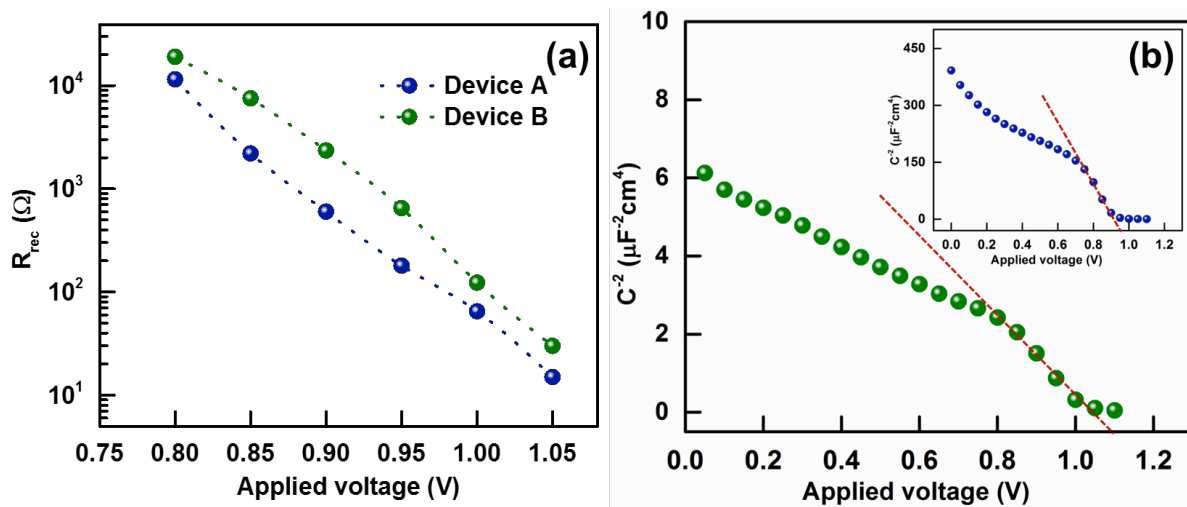
Figure 4. (a) Variation of recombination resistance as a function of applied voltage, and (b) Mott-Schottky plots of the triple (Device A) and quadruple (Device B) cation based perovskite solar cells.
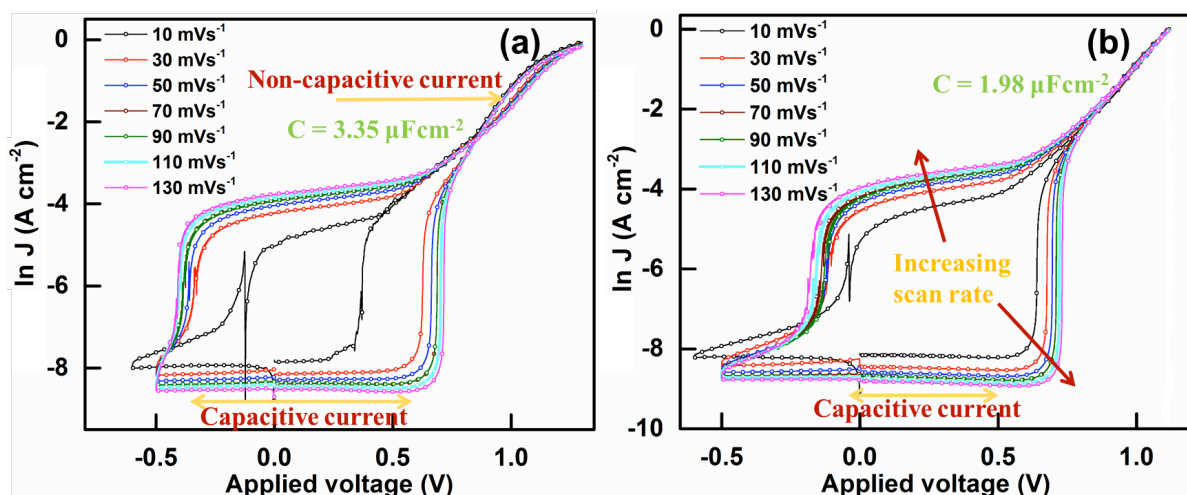
Figure 5. J-V characteristics at different scan rates with logarithmic current for (a) triple (Device A) and (b) quadruple (Device B) cation based perovskite solar cells.

To explore the role of Rb cations on the charge accumulation at the interfaces (with respect to the low frequency capacitance as measured by the IS spectra), J-V characteristics as a function of scan rate (Figure 5a and b) for both solar cells were measured in dark within the bias range of -0.5-1.4 V in the forward and reverse directions. In both solar cells, the net J-V response, which exhibits a shape like a square loop, follows the same trend in the low forward bias and merges to a single line as the bias approaches a higher value. However, magnitude of the current (I_{SC}) and area under the square loop are different for both systems, which perhaps stems form the difference in the interfacial charge accumulation. A similar trend was shown by Almora et al. for $CH_3NH_3PbI_3$ devices with different selective contacts by assuming a voltage independent capacitance i.e., $J_{cap} = dQ/dt = C\, dV/dt = Cs$ where, J_{cap} is the excess current to the equilibrium current by $J_{cap} = J - J_0$. [36] The net J-V response expression discussed in the context of Figure 2 is modified by the excess term i.e., hysteretic current (J_H). The J_H contains the contribution from both capacitive and non-capacitive current (J_{nonC}). J_{cap} is generally observed in the low and mid bias range, and at a high scan rate it is limited by the interfacial capacitive time constant. On the other hand, J_{nonC} appears at a low sweep rate and is expressed as $J_{nonC} = J_{max}\left[1 + exp\left(-q\frac{(V-V_0)}{mk_BT}\right)\right]^{-1}$, where, J_{max} is the current attained at a high potential. [36] The variation in J_{cap} with changing sweep rate is shown in SI (Figure S4) with a constant capacitance values of 3.35 and 1.98 μFcm^{-2}, respectively, for the device A and B. It is worth mentioning that the same quality of selective contact in both devices with a lower value of capacitance in device B (Rb containing perovskite) suppresses the interfacial traps. To further confirm these observations, capacitance versus frequency measurement was carried out under the short circuit conditions (Figure S5). The spectra obtained at the low and intermediate frequency region for both device exhibit two distinguishable capacitance trends. The device A has a higher value of capacitance at a low

frequency than the device B; similar to the observations from Figure S5. In general, the low frequency capacitance is ascribed to the interfacial phenomenon i.e., ionic and electronic charge accumulation at the interfaces involving selective contacts. [6] From the above discussion, we conclude that Rb cation (device B) suppresses the defects/traps at the TiO_2/perovskite interface and the anomalous hysteresis. It has been reported that the hysteresis in J-V characteristics is closely related to the intrinsic property of a semiconductor, whereas, some studies also show a correlation between the ionic transport and band bending in the bulk perovskite. Reports regarding controlling the interfaces between the selective contact and the perovskite layer by employing inverted structure, passivation layer, Li treatment, etc. have been documented. [19-22,37-41] However, we demonstrate the impact of composition (Rb) of perovskite on the interfacial properties and hysteresis, which renders our study highly pertinent.

In summary, using a combination of techniques, we have successfully unraveled the reasons that have led to the realization of higher photovoltaic performance when an extra cation (Rb) was incorporated into the absorber films. In addition to high V_{OC}, a relatively better performing device based on Rb possesses a higher value of *FF*, which arises from the coupled influence of the low recombination, low resistance offered to holes at the perovskite/spiro-OMeTAD interface (lower impedance element in the high frequency) and low series resistance (R_S). The dark JV characteristics with scan rate measurements established that a lower value of charge storage in a relatively more efficient device (containing Rb cation) could be ascribed to a fewer number of interfacial reactive sites. This study provides a thorough understanding of impact of the chemical composition of perovskite layer on the interfacial properties of highly efficient devices, and also highlights new strategies to elucidate the high-performance multiple-cation PSCs.

11

Experimental Section

Preparation of TiO$_2$ photoanode. Fluorine-doped tin oxide (FTO)-glass substrates (TCO glass, NSG 10, Nippon sheet glass, Japan) were cleaned by ultrasonication in Hellmanex (2%, deionized water), rinsed thoroughly with de-ionized water and ethanol, and then treated in oxygen plasma for 15 min. A compact layer of TiO$_2$ of ca 30 nm was subsequently deposited via spray pyrolysis at 450 °C using a commercial titanium diisopropoxide bis(acetylacetonate) solution (75% in 2-propanol, Sigma-Aldrich) diluted in anhydrous ethanol (1:9, volume ratio) as precursor and oxygen as a carrier gas. A mesoporous TiO$_2$ layer was deposited by spin coating a diluted paste (1:6 wt. ratio) (Dyesol 30NRD: ethanol) (4000 rpm, acceleration 2000 rpm for 20 s) onto the substrate containing TiO$_2$ compact layer. This was followed by a series of sintering steps (325 °C for 5 min with 15 min ramp time, 375 °C for 5 min with 5 min ramp time, 450 °C for 30 min with 5 min ramp time) in dry air. For Li treatment of mesoporous TiO$_2$ photoanode, 150 μL of bis(trifluoromethylsulfonyl)imide lithium salt (LiTFSI) solution in acetonitrile (10mg/mL, freshly prepared in argon atmosphere) was spin coated (3000 rpm, acceleration 2000 rpm for 20 s) after a loading time of 10 s. Thereafter, Li treated substrates were subjected to second sintering step at 450 °C for 30 min.

Deposition of multiple cation based perovskite films. The perovskite films were deposited using single-step deposition method from the precursor solution containing FAI (1M), PbI$_2$ (1.1 M), MABr (0.2 M) and PbBr$_2$ (0.2 M) in anhydrous dimethylformamide/ dimethylsulphoxide (4:1 (volume ratio)). Thereafter, 5% of CsI (abcr GmbH) (1.5 M DMSO) and/or 5% of RbI (Sigma Aldrich), (1.5 M DMF: DMSO, 4:1 volume ratio) was added to the perovskite precursor solution. The precursor solution was spin-coated onto the mesoporous TiO$_2$ films in a two-step programme at 1000 and 6000 r.p.m. for 10 and 30 s, respectively. During the second step, 100 μl of chlorobenzene was dropped on the spinning substrate 10 s prior to the end of the programme. This was followed by annealing the films at 100 °C for 60

min. The device fabrication was carried out under controlled atmospheric conditions with humidity <1%.

Deposition of hole conductor. To complete the fabrication of devices, 2,2',7,7'-tetrakis(*N*,*N*-di-*p*-methoxyphenylamine)-9,9-spirobifluorene (spiro-OMeTAD, 60 mM in chlorobenzene), was deposited by spin coating 40 μL of the prepared solution at 4000 rpm for 20 s. Spiro-OMeTAD was doped with bis(trifluoromethylsulfonyl)imide lithium salt, tris(2-(1H-pyrazol-1-yl)-4-tert-butylpyridine)- cobalt(III) tris(bis(trifluoromethylsulfonyl) imide) (FK 209, Dynamo) and 4-tert-Butylpyridine in a molar ratio of 0.5, 0.05 and 3.3, respectively. Finally, ~70 nm gold (Au) layer was thermally evaporated.

Device characterization. The current-voltage (J-V) characteristics of the perovskite devices were recorded with a digital source meter (Keithley model 2400, USA). A 450 W xenon lamp (Oriel, USA) was used as the light source for photovoltaic (*J-V*) measurements. The spectral output of the lamp was filtered using a Schott K113 Tempax sunlight filter (Präzisions Glas & Optik GmbH, Germany) to reduce the mismatch between the simulated and actual solar spectrum to less than 2%. The photo-active area of $0.16 \ cm^2$ was defined using a dark-coloured metal mask. AC measurements were performed using a potentiostat Biologic SP300 equipped with a frequency response analyser. IS measurements were performed in the DC bias range of 0 to open circuit voltage with an AC perturbation signal of 10 mV in the frequency range of 1 Hz to100 kHz.

Elemental analysis: X-ray photoelectron spectroscopy (XPS) was performed on an X-ray photoelectron spectrometer (ESCALAB 250Xi, Thermo Fisher SCIENTIFIC INC., USA) with Al Kα radiation (hν = 1486.6 eV) as the source.

Supporting Information

Nyquist spectra, electrical equivalent circuit, variation in J_{cap} capacitance versus frequency measurements and XPS data. Supporting Information is available from the Wiley Online Library or from the author.

Acknowledgements

REFERENCES

1.   A. Kojima, K. Teshima, Y. Shirai, T. Miyasaka, *J. Am. Chem. Soc.* **2009**, *131*, 6050.

2.   http://www.nrel.gov/ncpv/images/efficiency_chart.jpg.

3.   D. Bi, W. Tress, M. I. Dar, P. Gao, J. Luo, C. Renevier, K. Schenk, A. Abate, F. Giordano, J.-P. Correa Baena, J.-D. Decoppet, S. M. Zakeeruddin, M. K. Nazeeruddin, M. Grätzel and A. Hagfeldt, *Sci. Adv.*, **2016**, *2,* 150117.

4.   M. I. Dar, G. Jacopin, S. Meloni, A. Mattoni, N. Arora, A. Boziki, S. M. Zakeeruddin, U. Rothlisberger, M. Grätzel, *Sci. Adv.* **2016**, *2,* e1601156.

5.   M. M. Lee, J. Teuscher, T. Miyasaka, T. N. Murakami, H. J. Snaith, *Science* **2012**, *338*, 643.

6.   J. Carrillo, A. Guerrero, S. Rahimnejad, O. Almora, I. Zarazua, E. Mas-Marza, J. Bisquert and G. Garcia-Belmonte, *Adv. Energ. Mater.*, **2016**, *6*, 1502246.

7.   A. Guerrero, J. You, C. Aranda, Y. S. Kang, G. Garcia-Belmonte, H. Zhou, J. Bisquert and Y. Yang, *ACS Nano*, **2016**, *10*, 218.

8.   N. J. Jeon, J. H. Noh, W. S. Yang, Y. C. Kim, S. Ryu, J. Seo, S. I. Seok, *Nature 517, 476-480 (2015).*

9.   H.-S. Kim, C.-R. Lee, J.-H. Im, K.-B. Lee, T. Moehl, A. Marchioro, S.-J. Moon, R. Humphry-Baker, J.-H. Yum, J. E. Moser, M. Grätzel, N.-G. Park, *Sci. Rep. 2012, 2, 591:1.*

10.   J. Choi, S. Song, M. T. Hörantner, H. J. Snaith and T. Park, *ACS Nano*, **2016**, *10*, 6029.

11.   H. Choi, C.-K. Mai, H.-B. Kim, J. Jeong, S. Song, G. C. Bazan, J. Y. Kim and A. J. Heeger, *Nat. Comm.*, **2015**, *6*, 7348.

12.   F. Giordano, A. Abate, J. P. Correa Baena, M. Saliba, T. Matsui, S. H. Im, S. M. Zakeeruddin, M. K. Nazeeruddin, A. Hagfeldt and M. Graetzel, *Nat. Comm.*, **2016**, *7*, 10379.

13.   Q. Wang, C. Bi and J. Huang, *Nano Energ.*, **2015**, *15*, 275.

14.   J. Seo, N. J. Jeon, W. S. Yang, H.-W. Shin, T. K. Ahn, J. Lee, J. H. Noh and S. I. Seok, *Adv. Energ. Mater.*, **2015**, *5*, 1501320.

15.   J. H. Kim, P.-W. Liang, S. T. Williams, N. Cho, C.-C. Chueh, M. S. Glaz, D. S. Ginger and A. K. Y. Jen, *Adv. Mater.*, **2015**, *27*, 695.

16.   A. K. Jena, H.-W. Chen, A. Kogo, Y. Sanehira, M. Ikegami and T. Miyasaka, *ACS App. Mater. Inter.*, **2015**, *7*, 9817.

17. Y. Zhang, M. Liu, G. E. Eperon, T. C. Leijtens, D. McMeekin, M. Saliba, W. Zhang, M. de Bastiani, A. Petrozza, L. M. Herz, M. B. Johnston, H. Lin and H. J. Snaith, *Mater. Horiz.*, **2015**, *2*, 315.

18. W. Tress, N. Marinova, T. Moehl, S. M. Zakeeruddin, M. K. Nazeeruddin and M. Gratzel, *Energ. Env. Sci.*, **2015**, *8*, 995.

19. J. Shao, S. Yang, L. Lei, Q. Cao, Y. Yu and Y. Liu, *Chem. Mater.*, **2016**, *28*, 7134.

20. F. Zhang, W. Ma, H. Guo, Y. Zhao, X. Shan, K. Jin, H. Tian, Q. Zhao, D. Yu, X. Lu, G. Lu and S. Meng, *Chem. Mater.*, **2016**, *28*, 802.

21. D. Yang, X. Zhou, R. Yang, Z. Yang, W. Yu, X. Wang, C. Li, S. Liu and R. P. H. Chang, *Energ. Env. Sci.*, **2016**, *9*, 3071.

22. L. Zhao, X. Wang, X. Li, W. Zhang, X. Liu, Y. Zhu, H.-Q. Wang and J. Fang, *Sol.Energ. Mater. Sol. Cells*, **2016**, *157*, 79.

23. M. Saliba, T. Matsui, J.-Y. Seo, K. Domanski, J.-P. Correa-Baena, M. K. Nazeeruddin, S. M. Zakeeruddin, W. Tress, A. Abate, A. Hagfeldt and M. Gratzel, *Energ. Env. Sci., 2016, 9, 1989.*

24. M. Saliba, T. Matsui, K. Domanski, J.-Y. Seo, A. Ummadisingu, S. M. Zakeeruddin, J.-P. Correa-Baena, W. R. Tress, A. Abate, A. Hagfeldt and M. Grätzel, *Science, 2016, 10.1126/science.aah5557.*

25. H. Tao, W. Ke, J. Wang, Q. Liu, J. Wan, G. Yang and G. Fang, *J. Pow. Sour.*, **2015**, *290*, 144.

26. W. Ke, G. Fang, J. Wan, H. Tao, Q. Liu, L. Xiong, P. Qin, J. Wang, H. Lei, G. Yang, M. Qin, X. Zhao and Y. Yan, *Nat. Comm.*, **2015**, *6*, 6700.

27. L. Gouda, R. Gottesman, A. Ginsburg, D. A. Keller, E. Haltzi, J. Hu, S. Tirosh, A. Y. Anderson, A. Zaban and P. P. Boix, *J. Phys. Chem. Lett.,* **2015**, *6*, 4640.

28. G.-J. A. H. Wetzelaer, M. Scheepers, A. M. Sempere, C. Momblona, J. Ávila and H. J. Bolink, *Adv. Mater.*, **2015**, *27*, 1837.

29. J. Shi, X. Xu, D. Li and Q. Meng, *Small*, **2015**, *11*, 2472.

30. T. Kirchartz, F. Deledalle, P. S. Tuladhar, J. R. Durrant and J. Nelson, *J. Phys. Chem. Lett.*, **2013**, *4*, 2371.

31. A. Pockett, G. E. Eperon, T. Peltola, H. J. Snaith, A. Walker, L. M. Peter and P. J. Cameron, *J. Phys. Chem. C*, **2015**, *119*, 3456.

32. A. Todinova, J. Idígoras, M. Salado, S. Kazim and J. A. Anta, *J. Phys. Chem. Lett.*, **2015**, *6*, 3923.

33. E. Guillén, F. J. Ramos, J. A. Anta and S. Ahmad, *J. Phys. Chem. C*, **2014**, *118*, 22913.

34. E. J. Juarez-Perez, M. Wußler, F. Fabregat-Santiago, K. Lakus-Wollny, E. Mankel, T. Mayer, W. Jaegermann and I. Mora-Sero, *J. Phys. Chem. Lett.*, **2014**, *5*, 680.

35. Y. Liu, M. Bag, L. A. Renna, Z. A. Page, P. Kim, T. Emrick, D. Venkataraman and T. P. Russell, *Adv. Energ. Mater.*, **2016**, *6*, 1501606.

36. O. Almora, C. Aranda, I. Zarazua, A. Guerrero and G. Garcia-Belmonte, *ACS Energ. Lett.*, **2016**, *1*, 209.

37. M. I. Dar, M. Abdi-Jalebi, N. Arora, M. Grätzel and M. K. Nazeeruddin, *Adv. Energy Mater.* **2016,** *6*, 1501358.

38. C. Eames, J. M. Frost, P. R. F. Barnes, B. C. O'Regan, A. Walsh and M. S. Islam, *Nature Comm.* **2015**, *6*, 7497.

39. N. Arora, M. I. Dar, M. Hezam, W. Tress, G. Jacopin, T. Moehl, P. Gao, A. S. Aldwayyan, B. Deveaud, M. Grätzel, M. K. Nazeeruddin *Adv. Funct. Mater.* **2016,** *26*, 2846-2854.

40. S. van Reenen, M. Kemerink and H. J. Snaith, *J. Phys. Chem. Lett.*, **2015**, *6*, 3808.

41. B. Chen, M. Yang, S. Priya and K. Zhu, *J. Phys. Chem. Lett.*, **2016**, *7*, 905.

The confluence of the low trap-assisted charge carrier recombination, low resistance offered to holes at the perovskite/spiro-OMeTAD interface with the low series resistance (R_S) and a lower value of charge storage leads to the realization of higher photovoltaic performance when an extra cation (Rb) is incorporated into the perovskite absorber films.

Keywords perovskite solar cells, charge carrier recombination, impedance spectroscopy, interfacial properties

Pankaj Yadav, M. Ibrahim Dar, [*] *Neha Arora, Essa A. Alharbi, Fabrizio Giordano, Shaik Mohammed Zakeeruddin, Michael Grätzel*

Dr. P. Yadav, Dr. M. I. Dar, Dr. N. Arora, E. A. Alharbi, Dr. F. Giordano, Dr. S. M. Zakeeruddin, Prof. M. Grätzel
Laboratory of Photonics and Interfaces, Institute of Chemical Sciences and Engineering, École Polytechnique Fédérale de Lausanne, CH-1015-Lausanne, Switzerland.

E-mail: ibrahim.dar@epfl.ch

Understanding the role of rubidium in multiple-cation based high efficiency perovskite solar cells
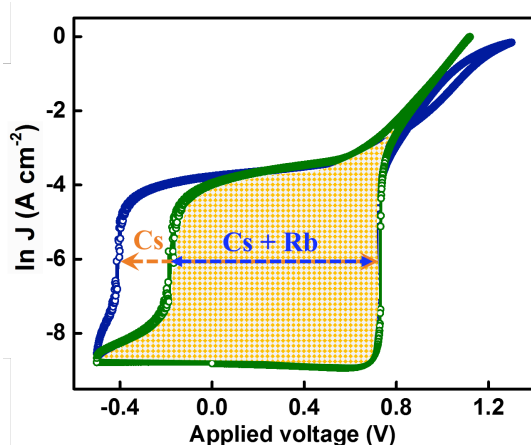
Supporting Information

Understanding the role of rubidium in multiple-cation based high efficiency perovskite solar cells

Pankaj Yadav, M. Ibrahim Dar, [*] *Neha Arora, Essa A. Alharbi, Fabrizio Giordano, Shaik Mohammed Zakeeruddin, Michael Grätzel*

Dr. P. Yadav, Dr. M. I. Dar, Dr. N. Arora, E. A. Alharbi, Dr. F. Giordano, Dr. S. M. Zakeeruddin, Prof. M. Grätzel
Laboratory of Photonics and Interfaces, Institute of Chemical Sciences and Engineering, École Polytechnique Fédérale de Lausanne, CH-1015-Lausanne, Switzerland.

E-mail: ibrahim.dar@epfl.ch
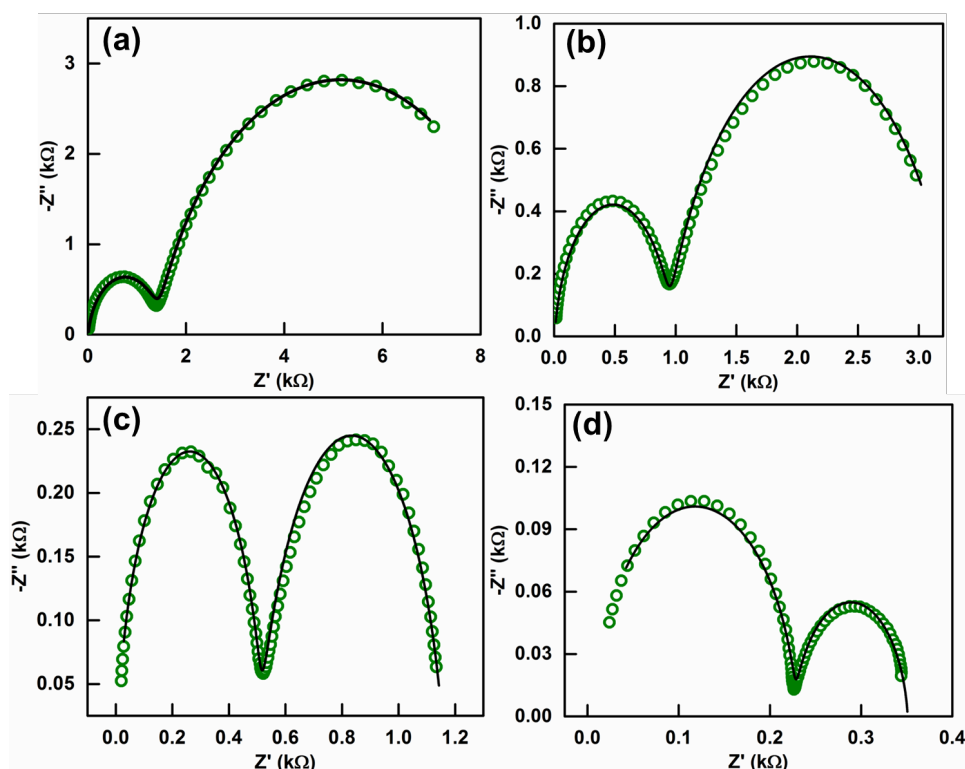
Figure S1. Selected Nyquist spectra recorded at different applied potentials from the quadruple (Device B) cation based perovskite solar cell, fitted with the equivalent circuit to show the appropriateness of the model; the symbols represent the experimental data and lines are the theoretical fits. (a) 0.8V, (b) 0.85 V, (c) knee voltage, and (d) open circuit voltage.
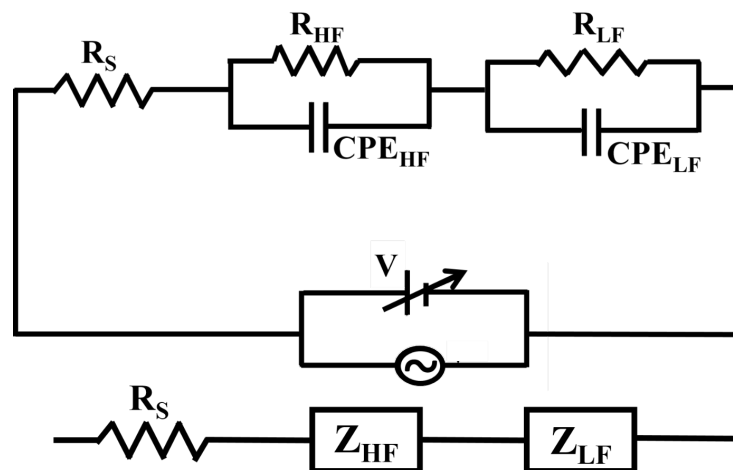
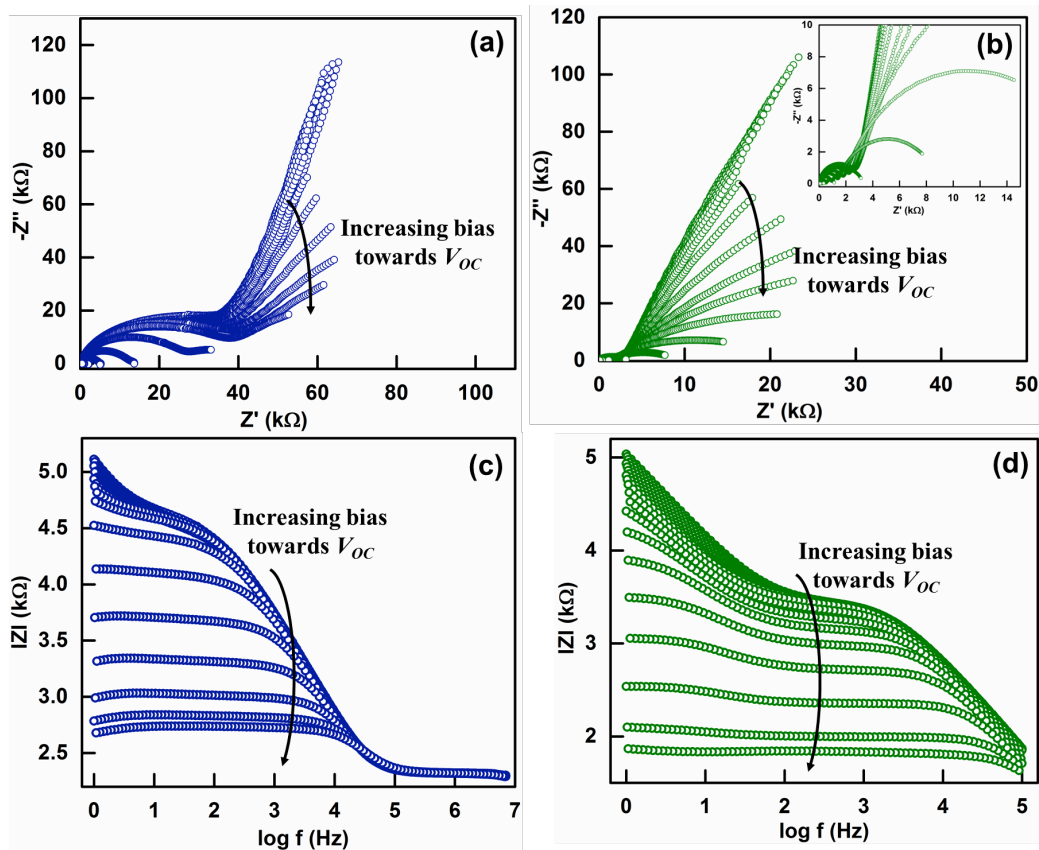**Figure S2.** Electrical equivalent circuit employed to fit the Nyquist spectra.

Figure S3. Nyquist spectra recorded at different applied potentials for (a) triple (Device A) and (b) quadruple (Device B) cation based perovskite solar cells, and Bode plots for (c) triple (Device A) and (d) quadruple (Device B) cation based perovskite solar cells recorded at different applied potentials.
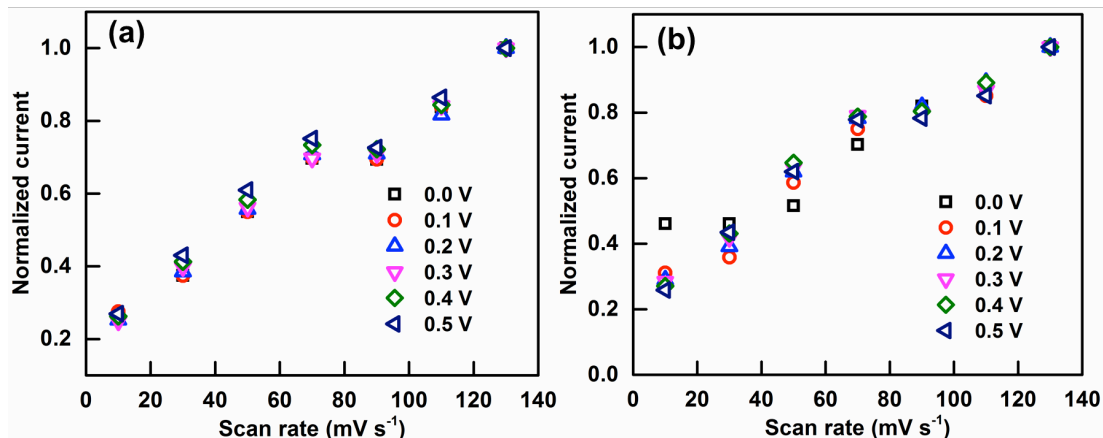
Figure S4. Variation in J_{cap} with the change in sweep rate for the triple (a) and quadruple (b) cation based perovskite solar cells.
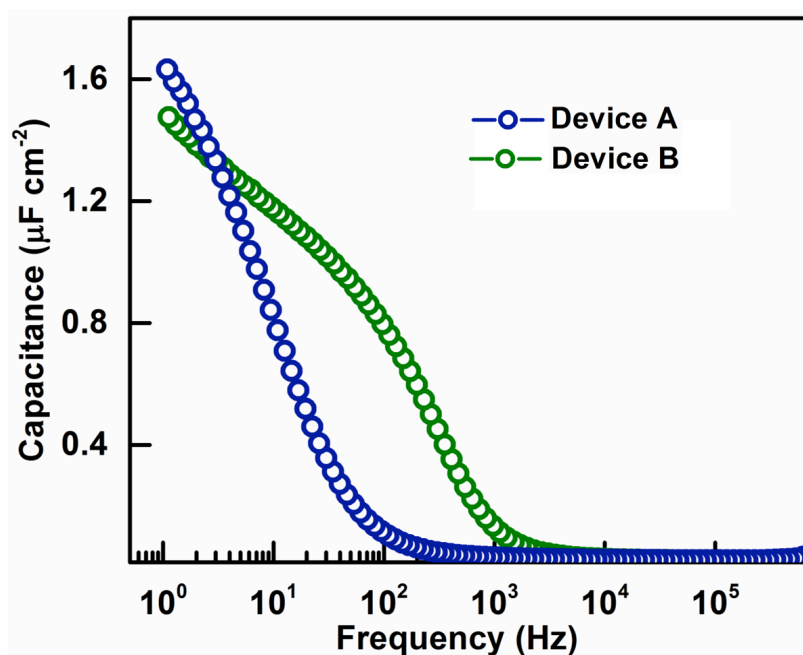

Figure S5. Capacitance versus frequency measurement carried out under short circuit conditions for the triple (Device A) and quadruple (Device B) cation based perovskite solar cells.
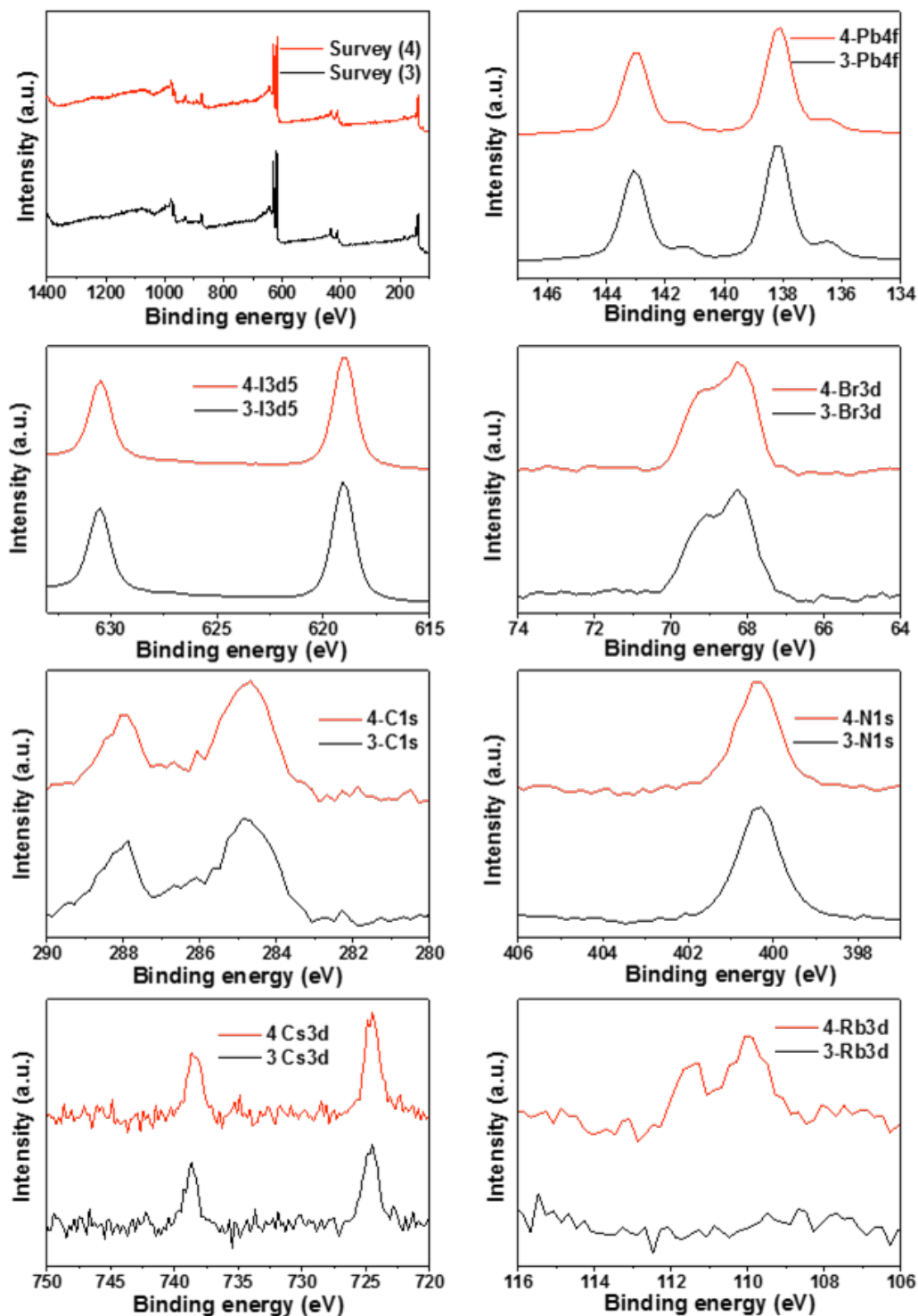
Figure S6. X-ray photoelectron spectroscopic (XPS) analysis of triple and quadruple cation based perovskite films.